

Free energy of Xe incorporation at point defects and in nanovoids and bubbles in UO₂

S. T. Murphy, A. Chartier, and L. Van Brutzel

CEA, DEN, DPC, SCCME, Laboratoire de Modélisation Thermochimique et Thermodynamique, F-91191, Gif-sur-Yvette, France

J.-P. Crocombette

CEA, DEN, DMN, Service de Recherches de Métallurgie Physique, F-91191, Gif-sur-Yvette, France

(Received 4 October 2011; published 5 April 2012)

Intra- and intergranular fission gas bubbles in nuclear fuels are known to have a deleterious effect on fuel performance, particularly at high levels of burnup. The mechanisms by which randomly distributed fission gas atoms agglomerate to form larger fission bubbles are not well understood. Therefore, this paper aims to examine the thermodynamics of bubble nucleation from isolated point defects to nanovoids and ultimately to bubbles of ≈ 2.0 nm using molecular-dynamics simulations employing empirical pair potentials. A thermodynamic driving force for bubble nucleation from point defects is highlighted by the substantial reduction in the free energy of Xe atoms contained within larger bubbles relative to accommodation at point defects. The simulations also illustrate the processes that the lattice surrounding a fission gas bubble undergoes in order to prevent thermal resolution, clearly indicating the thermodynamic imperative to ensure the Xe remains in the bubble.

DOI: [10.1103/PhysRevB.85.144102](https://doi.org/10.1103/PhysRevB.85.144102)

PACS number(s): 28.41.Ak

I. INTRODUCTION

Fluorite structured uranium dioxide (UO₂) is the fuel used most widely in the generation of electricity by nuclear power. As a direct consequence of the fission process, the concentration of uranium in the matrix is decreased and is replaced by daughter elements, including noble gases, such as krypton and xenon. The concentration of each of these fission products (FPs) in the fuel at any given time will depend on a number of factors, such as: (i) the age and use profile of the fuel (i.e., burnup), (ii) the type of reactor, (iii) the thermodynamic stability of the FP within the UO₂ matrix, and (iv) the activation energy for transport of the FP through the lattice. Point defects are of fundamental importance when considering all the factors mentioned above. The age, use profile, and type of reactor will dictate the relative concentrations of the point defects present, which will, in turn, influence the relative stability of the daughter products within the matrix and also the rate of diffusion through the lattice. This last phenomenon is important as it dictates the rate at which FPs, which are insoluble in the lattice, can precipitate to either the surface or the grain boundaries.

Commensurate with the importance of point defects in the accommodation of FPs, there has been a significant effort to determine point-defect concentrations, distributions, and properties in UO₂. Atomistic simulation, in its various guises, has shown itself to be particularly adept at providing this information. First, Grimes and Catlow¹ developed a comprehensive framework for the theoretical investigation of FP solution in UO₂. This and related papers²⁻⁵ established the differing concepts of incorporation energy and the related solution energy. The FP incorporation energy $E_{\text{inc}}(\text{FP})$ is defined as the energy to incorporate a FP on a preexisting point defect,

$$E_{\text{inc}}(\text{FP}) = E_{\text{def}}(\text{FP}_{\text{trap}}) - E_{\text{def}}(V_{\text{trap}}), \quad (1)$$

where $E_{\text{def}}(\text{FP}_{\text{trap}})$ is the defect energy of the FP located on a trap site and $E_{\text{def}}(V_{\text{trap}})$ is the defect energy of the preexisting trap [for incorporation at an interstitial site $E_{\text{def}}(V_{\text{trap}}) = 0$].

This is only valid when the concentration of trap sites is greater than the FP concentration. If the number of FPs exceeds the number of trap sites, the FPs must create trap sites at which to reside. Therefore, the energy required to create this defect, $E_f(\text{trap})$, has to be added to the incorporation energy in order to obtain a solution energy,

$$E_{\text{sol}}(\text{FP}) = E_{\text{inc}}(\text{FP}) + E_f(\text{trap}). \quad (2)$$

A positive value for the solution energy suggests that the FP is insoluble in the lattice.

The early empirical-potential-based simulation papers of Catlow² and then Grimes and Catlow¹ predicted that the lowest-energy process for Xe incorporation in stoichiometric UO₂ is for the Xe atom to sit in a charge neutral trivacancy defect or Schottky (Sch) defect (i.e., $[\text{V}_{\text{U}}''':2\text{V}_{\text{O}}^{\bullet}]^{\times}$ in Kröger-Vink notation)⁶ or in the negatively charged divacancy $[\text{V}_{\text{U}}''':\text{V}_{\text{O}}^{\bullet}]'$. The solution of Xe at the neutral Sch defect is predicted for hypostoichiometric urania (i.e., UO_{2-x}), however, in a hyperstoichiometric material (i.e., UO_{2+x}) solution at the cation vacancy is predicted to be the lowest-energy process. This change in behavior is due to a significant decrease in the formation energy of the uranium vacancy when the fuel is oxidized.

Early quantum-mechanical simulations of UO₂ failed to reproduce its insulating behavior.⁷ Despite this apparent limitation, Freyss *et al.*⁸ used density functional theory (DFT) and the generalized gradient approximation (GGA) to study Xe incorporation on different trap sites in UO₂. Their results predicted that the incorporation energy for Xe onto a uranium vacancy is lower than on a vacant oxygen or an interstitial site. These observations are in agreement with the previous empirical-potential-based papers but, unfortunately, due to computational constraints, defect clusters, such as the Sch defect were not considered. The DFT-GGA simulations of Yun *et al.*⁹ employed larger cells and enabled the incorporation of Xe into di- and trivacancies (i.e., Sch defects) to be studied. They found that the lowest-energy incorporation process is for the Xe atom to reside on a Sch defect. More

recent DFT + U simulations, which correctly predict UO_2 to be an insulator, suggest that the process with the lowest incorporation energy involves the neutral trivacancy.^{10,11} Furthermore, Nerikar *et al.*¹⁰ suggest that solution of Xe at Sch defects is the most favorable solution process for both stoichiometric and hypostoichiometric UO_2 , but as the oxygen concentration increases, the cation vacancy becomes the most thermodynamically stable solution site. More recent DFT simulations employing the GGA + U exchange-correlation functional predict that the divacancy is the lowest-energy incorporation and solution process.¹² Geng *et al.*¹³ suggest that the thermodynamic competition between $\text{Xe}_U^{\text{'''}}$ and $\text{Xe}_{\text{Sch}}^{\times}$ can be influenced indirectly by the presence of clustered oxygen defects.

Overall, there appears to be a broad consensus in the literature concerning the mode of xenon accommodation at point defects in UO_2 across a wide compositional range. What all of the computational investigations, mentioned above, have in common is that, independent of how the forces between ions are modeled (either via an empirical pair potential or quantum mechanically), they all employ energy minimization at 0 K to calculate the energy of the point defects. Temperature effects, when considered, are then taken into account using the point-defect models of Matzke¹⁴ and Lidiard¹⁵ and, therefore, are extrapolated from this energy value at 0 K.

Since xenon is predicted to be insoluble in UO_2 (Ref. 16), it may be expected that Xe atoms would migrate either toward the surface or to form either intra- or intergranular bubbles or planar clusters.¹⁷ A number of papers have attempted to understand the rate and mechanisms responsible for Xe nucleation in UO_2 . Moore *et al.*¹⁸ predicted the aggregation of isolated Xe atoms into a single large cluster from their molecular-dynamics (MD) simulations. The aggregation process observed was enhanced by the high concentration of Sch vacancy defects included in the simulations. Govers *et al.*¹⁹ studied the evolution of in-pile bubble distributions and estimated an activation energy for Xe diffusion of 0.9 eV. This value is significantly lower than the 3.9 eV determined from out-of-pile experiments by Cornell²⁰ and the value of ~ 3.9 eV observed in an unirradiated sample.²¹ Atomistic simulation, employing interatomic potentials²² and DFT²³ has been used to examine the different diffusion mechanisms for Xe migration in $\text{UO}_{2\pm x}$. For stoichiometric UO_2 , an activation energy of 4.5 eV was obtained using the empirical potentials²² in good agreement with the 3.9 eV of Matzke,²¹ and values between 4.99 and 6.56 eV were obtained using DFT.²³ The simulations examined the role of point defects in facilitating Xe transport through otherwise pristine UO_2 , therefore, they provide a good comparison with the unirradiated sample. Mechanisms for Xe resolution into the lattice have also been discussed.^{24–27}

Fission gas bubbles measuring up to 12 Å in radius have been observed at relatively low burnups of up to 18 $\text{GW}^{-1} \text{d}^{-1} \text{t}$.^{28,29} Similarly sized bubbles have also been observed using TEM in UO_2 irradiated with Xe^{3+} ions.³⁰ At much higher burnups, these bubbles coalesce to form larger fission bubbles. High-resolution TEM observations on high-burnup fuels suggest fission bubbles can become as large as 100 Å in diameter with Xe densities of 3.8–6.0 g cm^{-3} (0.029–0.046 mol cm^{-3} or a Xe:Sch ratio of 0.7–1.2) consistent with the presence of Xe in its solid form.³¹ Martin *et al.*³²

observe small nanometer-sized Xe aggregates containing solid Xe with a cell parameter of 5.61 ± 0.02 Å.

Traditionally, either the van der Waals equation or the ideal-gas law has been used to describe the equation of state of fission gases in nuclear fuels, however, these models have been found to provide an inadequate description for the overpressurized gas bubbles found in the rim structure of high-burnup nuclear fuel pellets.³³ A number of simulation papers have extended the equation of state for Xe into the high-temperature and pressure regimes expected in a nuclear reactor.^{33–35} The papers of Parfitt and Grimes²⁴ and Xiao-Feng *et al.*³⁶ used MD simulations of pure Xe with the same densities of gas atoms contained within their bubbles in UO_2 to estimate the pressure inside the bubble. Unfortunately, this ignores the impact of gas-crystal interactions, and a more explicit investigation of the equation of state of xenon contained in bubbles in UO_2 is essential.

Therefore, the goal of this paper is to investigate the free energy of Xe incorporated in point defects and in bubbles of increasing size and to compare the equation of state for Xe in gas bubbles in UO_2 as a function of bubble density and temperature.

II. METHODOLOGY

In our simulations, the lattice is treated as an array of point charges that interact via a combination of a Coulombic interaction and a parametrized short-range pair potential. There have been a large number of pair potentials developed for the UO_2 system,^{1,37–46} and recently, there has been some effort to evaluate their relative performance.^{47,48} For this paper, the Morelon potential⁴⁰ has been selected since this potential has been optimized for the study of point defects. This potential has been implemented successfully to examine radiation damage from single^{49–51} and overlapping radiation damage cascades in single-crystal UO_2 (Ref. 52) as well as to investigate radiation damage in polycrystalline UO_2 .^{53,54} Xe-Xe interactions were modeled using the potential developed by Tang and Toennies,⁵⁵ which is based on an accurate description of the van der Waals interactions calculated with different *ab initio* methods. The Xe-U and Xe-O interactions are of the Buckingham form with the parameters developed by Chartier *et al.*⁵⁶ by fitting to xenon incorporation energies at point defects in UO_2 calculated using DFT.

In a MD simulation, the forces on every ion in the supercell are calculated, and the ions/atoms are allowed to move under the influence of this force for a finite time period (in our simulations, this was 1 fs). This process is repeated iteratively, thus, allowing the time-dependent evolution of the lattice to be followed. A series of cavities of increasing size were then created by removing a number of Sch defects (i.e., one uranium atom and two oxygen ions), thus, maintaining overall charge neutrality. Furthermore, a Xe atom in a Sch defect represents the reference state for an unclustered Xe atom in the lattice. The smallest cavity to be studied, termed a nanovoid here, consisted of four Sch defects with the configuration optimized to ensure the largest possible free volume in the void (creation of the nanovoid will be discussed in more detail later). Larger cavities were created by removing all uranium and oxygen ions within a sphere of radius r_b centered on a uranium ion. Oxygen ions

TABLE I. Table showing the details of our MD simulations.

Property	Point defect	Nanovoid	Small bubble	Large bubble
Supercell	5 × 5 × 5	5 × 5 × 5	10 × 10 × 10	20 × 20 × 20
Number of ions	1500	1500	12 000	96 000
Initial radius/Å			6.0	10.0
Sch defects in cavity	NA ^a	4	19	121
Number of Xe	1	7	57	124

^aNA stands for not applicable.

were then added/removed at random to/from the surface of the bubble to ensure that the total number of oxygen ions removed was exactly twice the number of uranium ions removed. Two bubbles of different radii were used in this paper, a smaller and a larger bubble with radii of 6 Å in a cell containing 12 000 ions and a 10-Å bubble in a supercell containing 96 000 ions, respectively. From here on, these two bubbles are referred to as the small and large bubbles, respectively, although it should be noted that, in the fuel, both these bubbles would be considered to be small. Xe atoms were introduced randomly onto the now vacant UO₂ lattice sites within the cavity. A summary of all the simulation details employed herein is given in Table I.

All systems studied were equilibrated for 10 ps (10 000 time steps) under constant temperature and pressure conditions using the Nose-Hoover thermo- and barostats. The average lattice parameters, during the second half of this simulation, were then used to create a new supercell that was allowed to equilibrate under constant temperature and volume conditions using the Langevin thermostat for a further 20 ps (20 000 time steps). Once this equilibration was completed, the free energy of each Xe atom in the system was determined.

In order to calculate the free energy of a Xe atom located at a point defect or in a bubble, we perform an unusual disintegration procedure.⁵⁷ This disintegration procedure has been used previously to investigate He solubility in β-SiC.⁵⁸ The procedure is the conceptual opposite of the particle-insertion method suggested by Widom⁵⁹ in which an atom is gradually introduced into the simulation cell. As MD is discretized in time, the insertion proceeds step by step, and slowly, therefore, the number of steps required to perform the insertion is large. The disintegration method is simply the opposite in which a selected atom is removed slowly from the simulation cell. Below, we briefly recall why these procedures do indeed lead to an estimation of the free energy of an atom.

The premise of the particle-insertion method is that, when an atom is inserted randomly into a system in thermodynamic equilibrium, the change in the internal energy dU of the system can be calculated from Eq. (3),

$$dU = dF + T \delta S, \quad (3)$$

where dF is the change in the Helmholtz free energy, T is the temperature, and dS is the concomitant change in entropy. Should this insertion procedure be conducted sufficiently slowly, the impact on the surrounding ions in a single time step is negligible, and the process can be deemed to be quasistatic. As this process is reversible, we can assume that there is no creation of entropy (i.e., $\delta S_{\text{created}} = 0$) during a given time step,

and the total change in entropy is simply that exchanged with the thermostat $\delta S_{\text{exchanged}}$, and Eq. (3) becomes

$$dU = dF + T \delta S_{\text{exchanged}} = dF + \delta Q_{\text{reversible}}, \quad (4)$$

where $\delta Q_{\text{reversible}}$ is the variation in heat during a reversible process. The variation in the internal energy during a reversible reaction may also be given by Eq. (5),

$$dU = \delta Q_{\text{reversible}} + \delta W_{\text{reversible}}, \quad (5)$$

where $\delta W_{\text{reversible}}$ is the work performed along the disintegration path. Combining Eqs. (4) and (5) gives Eq. (6) where the change in free energy is the work performed along the disintegration path,

$$dF = \delta W_{\text{reversible}}. \quad (6)$$

The simulation is performed under constant temperature and volume conditions using a Langevin thermostat, and the number of atoms in the simulation, other than the target atom, remains constant (i.e., $n_{j \neq i}$), then,

$$\begin{aligned} dF &= \sum_N^{j=1} \left(\frac{\delta F}{\delta n_j} \right)_{V,T,n_j} dn_j + \left(\frac{\delta F}{\delta T} \right)_{V,n} dT + \left(\frac{\delta F}{\delta V} \right)_{T,n} dV \\ &= \left(\frac{\delta F}{\delta n_i} \right)_{V,T,n_{j \neq i}} dn_i, \end{aligned} \quad (7)$$

therefore,

$$dF = \mu_i dn_i, \quad (8)$$

where μ_i is the free energy of atom i , consequently,

$$\mu_i dn_i = \delta W_{\text{reversible}}. \quad (9)$$

Hence, if an atom is randomly added to the system $dn_i = 1$, then

$$\mu_i = W_{\text{reversible}}. \quad (10)$$

As we are interested in the free energy of atoms in a specific position within the simulation supercell, it is not possible to insert an atom randomly. Therefore, we adopt a different approach, whereby a target atom is disintegrated or slowly is removed from the system and $dn_i = -1$ and

$$\mu_i = -W_{\text{reversible}}. \quad (11)$$

During our simulations, we determine the work generated reducing the Xe interactions with the neighboring atoms and then integrate this work along the disintegration path to calculate the free energy. In the work presented here, each of the Xe atoms in the system was disintegrated individually in a series of simulations all started from the same equilibrated system.

The quality of this procedure depends on the speed of the disintegration as $\delta S_{\text{created}}$ converges to zero as the difference in the interactions between the target atom and its surroundings after each step becomes increasing smaller. A value of 20 000 time steps (i.e., 20 ps) was found to be sufficient to ensure that the disintegration process was quasistatic. All simulations were conducted using the in-house MD code NDM.

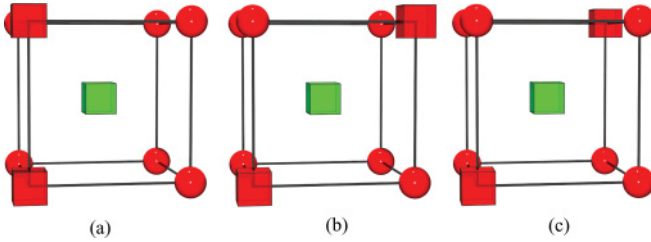


FIG. 1. (Color online) Diagrams showing the different arrangements of the Sch defect clusters (a) Sch 1, (b) Sch 2, and (c) Sch 3. The red spheres represent oxygen ions, and the red and green transparent cubes represent oxygen and uranium vacancies, respectively.

III. RESULTS AND DISCUSSION

A. Point defects

The first goal of this paper is to examine the free energy of Xe incorporation at point-defect trap sites in UO_2 . The defects considered are Xe_i^\times , Xe_U''' , Xe_O^\bullet , $\text{Xe}_{\text{dimer}}''$, and $\text{Xe}_{\text{Sch}}^\times$ where the three different initial configurations for the Sch trivacancy defects are considered (see Fig. 1). Xenon free energies for all of these defects at a number of temperatures are included in Table II. The Xe free energies of two ($2\text{Xe}_{\text{Sch}}^\times$) and three Xe ($3\text{Xe}_{\text{Sch}}^\times$) atoms incorporated into a single Sch defect also are included. For these two last calculations, the values of the free energies in Table II are the average over the three Sch defect configurations.

Table II shows the incorporation energies calculated using energy minimization with both the empirical pair potential and DFT and compares these with the free energies determined using the disintegration technique for temperatures up to 1300 K. There is a good level of agreement between the incorporation energies predicted using the empirical potential and the DFT for simple Xe solution sites (i.e., Xe_i , Xe_U''' , and Xe_O^\bullet). This result is not surprising as the Xe-O and Xe-U potential parameters were fitted using these defects.⁵⁶ For the more complex defects (i.e., those involving clusters of vacancies), there is some discrepancy in the absolute energies, however, the overall ordering of the incorporation energies is predicted to be the same with both techniques predicting

that solution at the type-1 Sch defect (see Fig. 1) is the most energetically favorable process and that incorporation at an interstitial site is the least energetically favorable solution process. Importantly, Table II shows that the effect of temperature on the free energies of Xe accommodated at point defects in UO_2 is negligible as the results obtained from static energy minimization simulations are almost identical to the free energies obtained for Xe incorporated at the same trap site at temperatures up to 1050 K. This is not the case for Xe accommodated at an interstitial site where there is a relatively large difference (0.3 eV) between the energy-minimized value and the free energy at 300 K. The origin of this discrepancy is that the Xe_i^\times defect is metastable and evolves to give a Xe_O^\bullet defect with an O_i' defect bound to it. This process is described as part of a complex Xe diffusion pathway as discussed by Liu *et al.*⁶¹ At higher temperatures (> 1500 K), this Xe_i^\times displaces a neighboring uranium atom from its lattice site, so the Xe now resides on a $[\text{V}_U''':\text{V}_O^\bullet]'$ defect cluster with a uranium and oxygen interstitial bound to it, a process also observed in the simulations of Xiao-Feng *et al.*³⁶

Table II also shows that, for Xe solution at point defects, such as $\text{Xe}_{\text{Sch}1}^\times$ and $\text{Xe}_{\text{Sch}3}^\times$, there is a significant change in the Xe free energy for temperatures greater than 1050 K. This is due to the increased mobility of the oxygen sublattice at higher temperatures.^{62,63} Consequently, the arrangement of the oxygen vacancy defects surrounding the uranium vacancy defect will be altered such that the initial Xe incorporation site may no longer be present. Therefore, we limit our paper to temperatures up to and including 1050 K.

Upon incorporation of a second Xe atom in a single Sch defect, the free energy of the Xe atoms increases dramatically, especially at low temperatures. However, the incorporation of a third Xe atom does not impact the average free energy significantly.

B. Nanovoids

Small nanovoids consisting of a number of Sch defects are an intermediary step in the formation of larger fission bubbles.⁵⁶ In order to study this step in the bubble formation process, a small nanovoid consisting of four Sch defects was created. The choice of four Sch defects is due to this

TABLE II. Table showing the free energies of Xe atoms incorporated at point defects in UO_2 . The results were compared to data obtained using energy minimization (where there is no concept of temperature) where forces were evaluated using DFT and the empirical potential employed here.⁵⁶

Temperature/K	Free energy/eV								
	Xe_i^\times	Xe_U'''	Xe_O^\bullet	$\text{Xe}_{\text{dimer}}''$	$\text{Xe}_{\text{Sch}1}^\times$	$\text{Xe}_{\text{Sch}2}^\times$	$\text{Xe}_{\text{Sch}3}^\times$	$2\text{Xe}_{\text{Sch}}^\times$	$3\text{Xe}_{\text{Sch}}^\times$
DFT (0 K)	12.01 ^a	5.77 ^a	9.14 ^a		1.2 ^b	1.8 ^b	2.3 ^b		
Empirical (0 K)	11.92 ^c	5.40 ^c	9.34 ^c	4.87	4.21 ^c	4.64	4.82		
300	11.71	5.45	9.27	4.87	4.23	4.71	4.88	8.12	8.24
550	11.54	5.48	9.27	4.87	4.23	4.74	4.91	7.56	8.48
800	11.07	5.56	9.22	4.89	4.23	4.73	4.87	7.05	7.20
1050	10.81	5.56	9.14	4.82	4.24	4.77	4.77	7.18	7.11
1300	10.73	5.64	8.98	4.77	4.64	4.78	5.10	6.24	6.44

^aThe local-density approximation.⁵⁶

^bThe GGA + U approximation.⁶⁰

^cChartier *et al.*⁵⁶

being the minimum number required to create a topologically symmetric cavity. Four uranium atoms were removed such that the vacancies formed the vertices of a tetrahedron. Oxygen anions, which form cubes surrounding each uranium site, were then removed from the corners of any edge shared by the oxygen cubes surrounding two uranium vacancies. The final oxygen vacancy was created by removing one of the oxygen ions in a nearest-neighbor position with respect to one of the uranium vacancies. The initial configuration of the nanovoid is given in Fig. 2(a).

Figure 3 shows the average free energy of the Xe atoms plotted as a function of the Xe:Sch ratio for Xe atoms contained in the nanocavity for different temperatures ranging from 300 to 1050 K. The results show very little influence of the temperature on the free-energy values as already shown for the point defects. Therefore, in the following section, we only discuss the results obtained at 300 K. When a single atom is placed inside the cavity, it moves toward the central oxygen vacancy such that it minimizes its interaction with the UO_2 lattice. The free energy for a Xe atom accommodated as such is about 1.5 eV. When a second Xe atom is placed in the nanovoid, the repulsion between the Xe atoms forces them to reside on two of the vacant uranium sites with an average free energy of 3.88 eV. The third and fourth Xe atoms then reside on the remaining vacant uranium sites [as shown in Fig. 2(b)], and the free energies of these Xe atoms are roughly unchanged, 3.67 and 3.86 eV for three and four Xe atoms, respectively. The cavity is formed from four Sch defects, consequently, when there are four Xe atoms contained within the nanovoid, the Xe:Sch ratio is 1; therefore, this average value of 3.88 eV per Xe atom can be compared to the free energy of a single Xe atom accommodated in a single Sch defect of 4.21 eV. This value is indicated by the dashed line in Fig. 3. As the average free energy of the four Xe atoms accommodated in a Sch defect (i.e., the Xe:Sch ratio is 1 in both cases), we predict a thermodynamic driving force to nucleation that is independent of temperature.

Incorporation of further Xe atoms into the nanovoid results in a significant increase in the free energy of the Xe atoms contained within (roughly 2 eV per xenon atom). This increase in energy is due to the lack of an available vacant uranium site and an increase in the pressure inside the void. For those Xe:Sch ratios greater than 1, the average free energy per Xe atom is always larger than the free energy of a single Xe atom accommodated in a single Sch defect. Therefore, the thermodynamic driving force present for lower Xe:Sch ratios disappears. Consequently, one can expect that, in the real material, the configurations of Xe:Sch ratios greater than 1 are unlikely to occur in nanovoids. Nevertheless, despite this significant increase in the average xenon energy inside the cavity, we do not see any resolution of the xenon into the lattice. Interestingly, Fig. 3 shows that, when further Xe atoms are introduced into the cavity, the average free energy per Xe atom slightly decreases. This behavior appears counterintuitive as it would be expected that, as the pressure inside the bubble increases, there would be a concomitant increase in the average free energy of the Xe atoms. However, rather than xenon being resolved into the urania, as the pressure inside the bubble increases, the Xe atoms force oxygen ions in the region immediately surrounding the bubble into the lattice [as

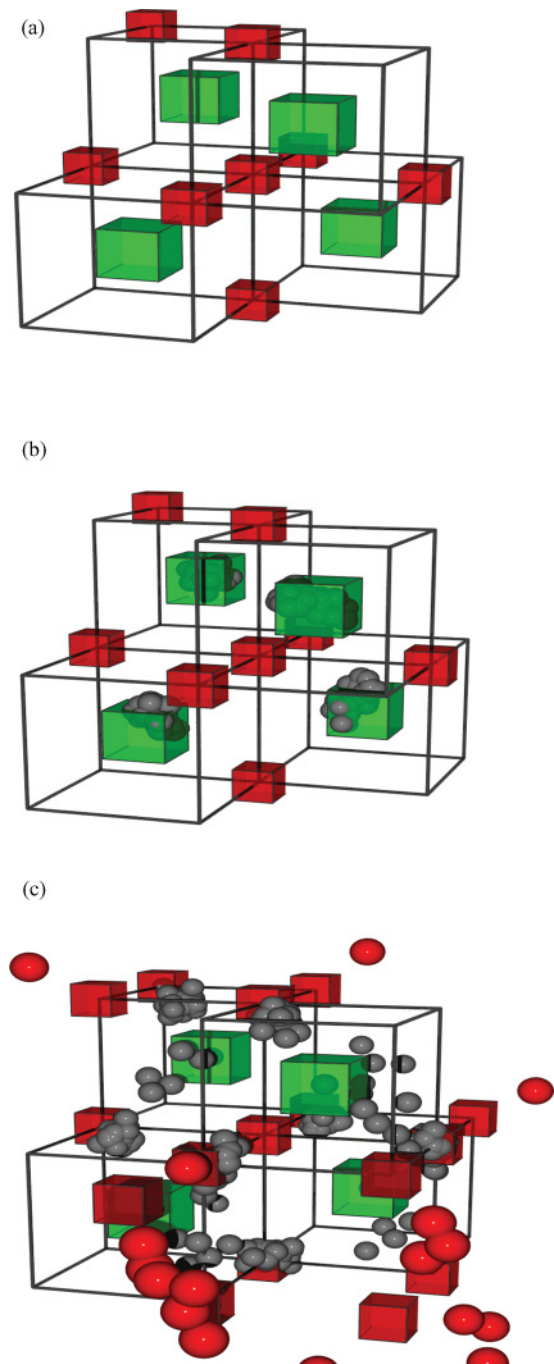


FIG. 2. (Color online) Diagrammatic representation of (a) an empty nanovoid (cavity) consisting of four Sch defects, (b) a nanovoid containing four Xe atoms, and (c) a nanovoid containing seven Xe atoms. The figures are a superposition of the simulation supercell with only the defect species shown. Transparent green and red cubes represent uranium and oxygen vacancies, respectively, and the red and gray spheres represent the average position of the oxygen interstitials and Xe atoms, respectively. In (c), the oxygen interstitials are the result of the oxygen ions surrounding the nanocavity being forced off their lattice sites, thus, increasing the size of the void.

shown in Fig. 2(c)], thus, increasing the size of the cavity itself and, subsequently, reducing the internal pressure in the void. As a result, there is no resolution observed in our simulations of nanovoids.

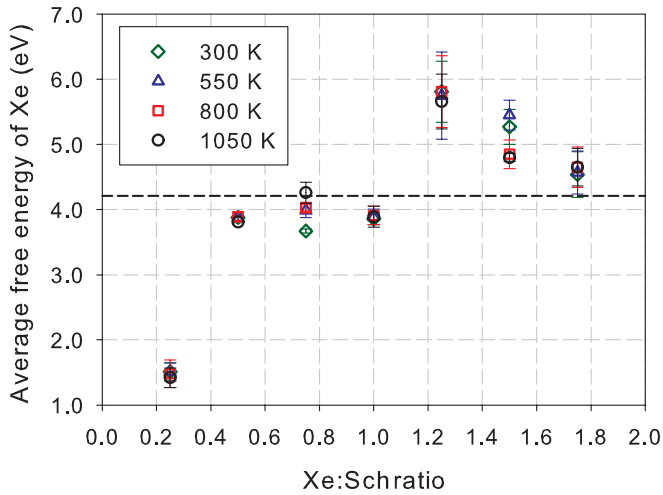


FIG. 3. (Color online) Plot showing the Xe free energy as a function of the Xe:Sch ratio for different temperatures ranging from 300 to 1050 K. The dashed line at 4.21 eV indicates the free energy found for one Xe atom accommodated in a Sch defect.

C. Bubbles

Having established that there is a thermodynamic driving force for the nucleation of small nanovoids containing Xe atoms, for Xe:Sch ratios less than 1, we examine the Xe free energy in larger size bubbles. Figure 4 shows the average free energy over all Xe atoms contained within the small and large bubbles as a function of the Xe:Sch ratio. For the small bubble, the free energy was determined at 0.1, 300, and 1050 K, however, for the larger bubble, the free energy was only determined at 300 K due to computational restraints. Also included are the results obtained for the nanovoids from Fig. 3.

For both the small and the large bubbles, the average free energy of the Xe atoms inside the bubble increases linearly with the Xe:Sch ratio until the Xe:Sch ratio is ≈ 1.3 . For this range, the value of the average free energy per Xe atom is lower than the free energy of a single Xe atom accommodated in a single Sch defect. Therefore, as is the case for the nanovoid,

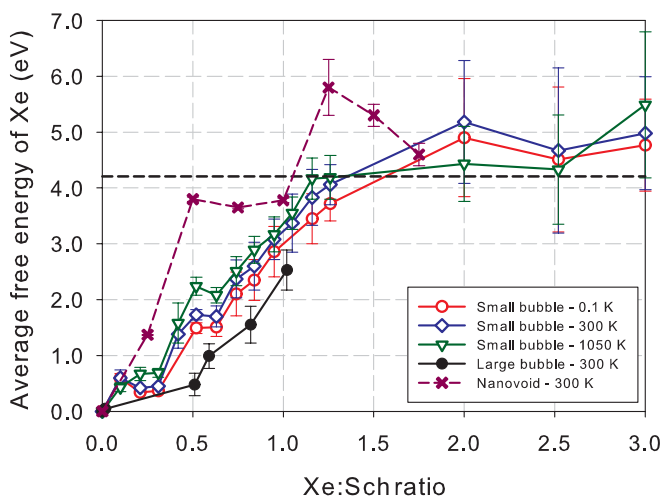


FIG. 4. (Color online) Plot showing the average free energy of xenon in bubbles in the UO_2 lattice as a function of the Xe:Sch ratio.

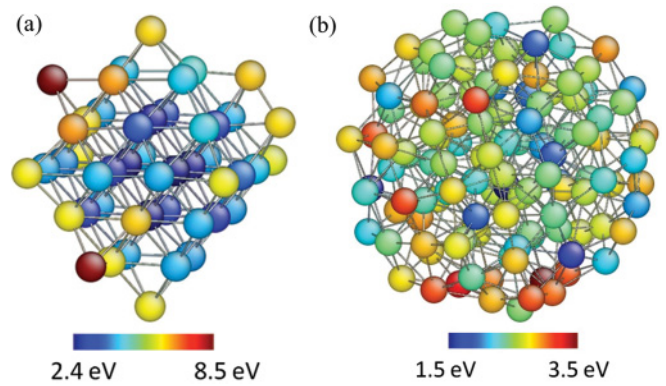


FIG. 5. (Color online) Spatial repartitions of Xe atoms contained within two different bubbles: (a) a small bubble of diameter 1.2 nm containing 48 Xe atoms (corresponding to a Xe:Sch ratio of 2.5) and (b) a large bubble of approximately 2.0 nm containing 120 Xe atoms (corresponding to a Xe:Sch ratio of 1.0). Each atom is colored according to its free energy.

there is a thermodynamic driving force, which yields to the nucleation of the Xe atoms. The intensity of this driving force decreases as the Xe:Sch ratio increases, i.e., as the Xe atom density in the bubble increases. Temperature appears to have only a very small effect on the free energy at a given Xe:Sch ratio. Furthermore, Fig. 3 shows that, as the size of the bubble increases, the average Xe free energy decreases for the same Xe:Sch ratio again suggesting a driving force to nucleation of bubbles up to 10 \AA in radius. This behavior is due to the existence of a boundary layer at the interface between the bubble and the UO_2 lattice inducing a specific spatial repartition of the Xe free energies. Figure 5(b) displays the 120 Xe atoms contained within the large bubble at 300 K corresponding to a Xe:Sch ratio of 1; the atoms have been color coded with respect to their free energies. In this figure, the Xe atoms with the highest free energies are concentrated at the surface of the bubble in contact with the UO_2 lattice. Therefore, since, for the larger bubbles, the ratio between the Xe atoms in the bubble core and the Xe atoms at the surface increases, the average free energy decreases as the bubble size increases. For Xe:Sch ratios higher than 1.3, the average free energy per Xe atom in the small bubble becomes almost constant and larger than the average free energy of a single Xe atom. This behavior is explained by two phenomena. The first is that, for these densities, the Xe atoms have formed a fcc solid as represented in Fig. 5(a), which displays 48 Xe atoms contained within the small bubble at 300 K corresponding to Xe:Sch = 2.5. The second phenomenon is that, as is the case for the nanovoids, the Xe atoms at the surface of the bubble create more space for themselves by forcing oxygen ions into the UO_2 lattice, thus, increasing the size of the bubble and keeping the Xe-Xe distance roughly constant.

Finally, we provide a comparison of the fission gas atoms contained within a bubble and pure xenon in order to discuss the importance of the gas-surface interaction. The free energy of pure xenon was determined by creating an entirely separate simulation supercell containing only Xe atoms. The density of Xe inside the bubble was controlled by changing the size of

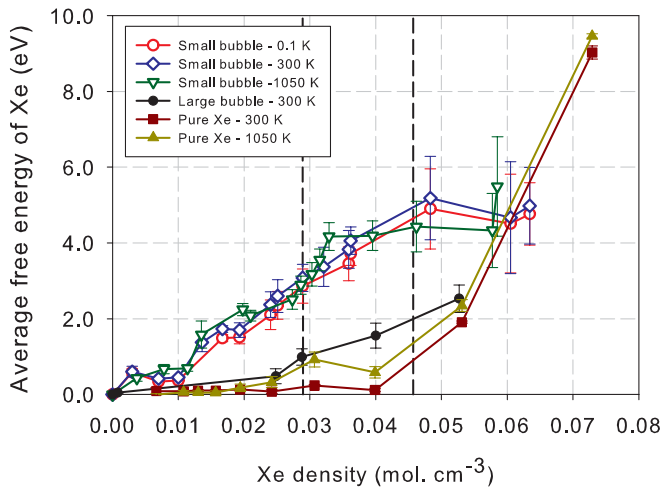


FIG. 6. (Color online) Plot showing the average free energy of xenon in bubbles in the UO_2 lattice as a function of the Xe density in the bubble. The average free energies determined for Xe atoms inside the bubbles are then compared with pure xenon. The vertical dotted lines represent the upper and lower bounds of the bubble density observed from the experiment.^{31,64}

the simulation supercell, and the simulations were performed as before without the initial constant pressure equilibration.

Figure 6 shows a comparison of the free energy of Xe within the cavities in UO_2 and in a pure Xe supercell as a function of the Xe density. Xe densities inside the cavities were determined by assuming that the bubbles were approximately spherical, and the radius was determined as the distance from the center of the bubble to the nearest U^{4+} or O^{2-} ion. The vertical dotted lines marked in Fig. 6 represent the upper and lower bounds of the estimated bubble densities from experiment.^{31,64}

As discussed in Sec. I, Chartier *et al.*⁵⁶ demonstrated the efficacy of the Xe-Xe interaction derived by Tang and Toennies⁵⁵ by plotting the equation of state and comparing with the experimental data of Beattie *et al.*⁶⁵ and Zisman *et al.*⁶⁶ Consequently, we are confident that the empirical potential acting between Xe atoms is accurate. For pure xenon, Fig. 6 shows that, at low densities, when the xenon is in a gaseous state, the average free energy is very close to zero at both 300 and 1050 K. At these low densities, the Xe atoms are sufficiently far apart that they are effectively noninteracting, and hence, their potential energy is effectively zero, thus, their total energy is equal to the atom's kinetic energy only. As the density increases, the Xe atoms begin to arrange themselves into a fcc solid. The phase change occurs at a density of $0.025 \text{ mol cm}^{-3}$ at 300 K and 0.03 mol cm^{-3} at 1050 K. After the onset of solidification, the free energy then decreases slightly as it approaches the equilibrium density for solid Xe at each temperature. Further increases in the density beyond the equilibrium value lead to a significant repulsive interaction between the Xe atoms, and consequently, the free energy increases dramatically as shown in Fig. 6. For the same Xe density in the supercell, the free energy is predicted to increase as a function of temperature.

Within the bubbles, the phase change from a gaseous Xe to a solid is retarded due to the surface of the urania restricting the rearrangement of the Xe atoms into the perfect fcc structure

(see Fig. 5), although the exact density at which solidification occurs is difficult to determine due to the small number of atoms involved. At higher pressures, the forces on the Xe atoms were sufficient to allow this rearrangement to occur on a MD time scale. The average free energy of the Xe atoms contained within the small bubble increases almost linearly with the density of the fission gas up until the free energy reaches $\approx 4.5 \text{ eV}$ at a bubble density of 0.04 mol cm^{-3} . This rate of increase in the free energy is substantially greater than for the pure Xe and reflects the interaction of the Xe atoms with the surface of the cavity. The rate at which the free energy increases as a function of Xe density in the small bubble appears to be independent of temperature.

A comparison of the free energy as a function of the density in the small bubble and the pure gas suggests that a model in which the Xe is considered to behave in a similar manner to pure Xe is inappropriate in bubbles of this size. At very high densities, the free energy plots for the small bubble and the free xenon converge, this represents the point at which the Xe is so dense that the surface interactions have a comparatively negligible effect on the free energy. For the large bubble in the low (i.e., $< 0.025 \text{ mol cm}^{-3}$) and the high (i.e., $> 0.54 \text{ mol cm}^{-3}$) density regions, the free energy is virtually identical to the pure Xe, however, in the intermediate region, there is still a small discrepancy. Unfortunately, this corresponds to the range of densities at which the bubbles are predicted to occur in the fuel, therefore, treating Xe contained in nuclear fuels as pure Xe may not be appropriate for bubbles of this size (i.e., $\approx 2 \text{ nm}$ in diameter), particularly at low temperatures.

IV. CONCLUSIONS

MD simulations employing empirical pair potentials have been used to study the free energy of Xe at point defects, in nanovoids, and in small bubbles in the UO_2 matrix. The conclusion drawn from the simulations of Xe incorporation at point defects shows that the most favorable trap site is the charge neutral Sch defect with the two oxygen ions residing on nearest-neighbor lattice sites, thus, maximizing the free volume available to the fission gas atom. This is in agreement with a wealth of other theoretical papers, both empirical and quantum mechanical. Temperatures up to 1050 K have been shown to have little or no effect on the free energy of Xe atoms incorporated at point defects, or bubbles in UO_2 , raising the possibility that defect formation energies determined using first-principles methods may be extrapolated at intermediate temperatures.

At no point in this paper was a Xe atom seen to undergo thermal resolution to the crystal matrix (i.e., thermal resolution does not occur on a MD time scale, however, it may occur at larger time scales). The processes that the lattice has to undergo in order to prevent resolution are evident from the point-defect simulations to the simulations of the largest bubbles. A Xe atom initially incorporated at an interstitial site in UO_2 was observed to displace an oxygen ion at low temperature and then to displace a neighboring uranium ion at high temperature, a process that has been observed elsewhere.³⁶ Similarly, when the pressure in the nanovoid or the bubble becomes sufficiently great, rather than undergo resolution, the Xe atoms force

oxygen ions from the bubble surface into the crystal lattice, thus, relieving the pressure inside the cavity as illustrated in Fig. 2(c).

Our simulations also demonstrate that there is a thermodynamic driving force to bubble nucleation. This thermodynamic driving force decreases linearly as the density inside the bubble increases and is greater for larger bubbles.

Finally, we have highlighted the limitations of a fuel-performance model that simply assumes the behavior of Xe gas inside small gas bubbles in nuclear fuels behaves in a similar manner to that of pure Xe. Whereas, this approximation may be valid for the largest of bubbles in the matrix due to

a significantly decreased surface-to-volume ratio, it clearly indicates that more work needs to be performed examining the equation of state of fission gas trapped in nuclear fuels.

ACKNOWLEDGMENTS

The authors would like to acknowledge funding through the European Commission under the FP7 F-Bridge project (Contract No. 211690). Computational resources were provided by the Centre de Calcul Recherche et Technologie (CCRT). Computer time was also provided as part of the GENCI challenge project (Allocation No. 2009-09c6149).

- ¹R. W. Grimes and C. R. A. Catlow, *Philos. Trans. R. Soc. London, Ser. A* **335**, 609 (1991).
- ²C. R. A. Catlow, *Proc. R. Soc. London, Ser. A* **364**, 473 (1978).
- ³R. G. J. Ball and R. W. Grimes, *J. Chem. Soc. Faraday Trans.* **86**, 1257 (1990).
- ⁴R. G. J. Ball and R. W. Grimes, *J. Nucl. Mater.* **188**, 216 (1992).
- ⁵S. Nicoll, H. Matzke, and C. R. A. Catlow, *J. Nucl. Mater.* **226**, 51 (1995).
- ⁶F. Kroger, *The Chemistry of Imperfect Crystals* (North-Holland, Amsterdam, 1964).
- ⁷J. P. Crocombette, F. Jollet, L. Thien Nga, and T. Petit, *Phys. Rev. B* **64**, 104107 (2001).
- ⁸M. Freyss, N. Vergnet, and T. Petit, *J. Nucl. Mater.* **352**, 144 (2006).
- ⁹Y. Yun, H. Kim, H. Kim, and K. Park, *J. Nucl. Mater.* **378**, 40 (2008).
- ¹⁰P. V. Nerikar, X.-Y. Liu, B. P. Uberuaga, C. R. Stanek, S. R. Phillpot, and S. B. Sinnott, *J. Phys.: Condens. Matter* **21**, 435602 (2009).
- ¹¹A. E. Thompson and C. Wolverton, *Phys. Rev. B* **84**, 134111 (2011).
- ¹²G. Brillant, F. Gupta, and Pasturel, *J. Nucl. Mater.* **412**, 170 (2011).
- ¹³H. Y. Geng, Y. Chen, Y. Kaneta, M. Kinoshita, and Q. Wu, *Phys. Rev. B* **82**, 094106 (2010).
- ¹⁴H. Matzke, *J. Chem. Soc., Faraday Trans. 2* **83**, 1121 (1987).
- ¹⁵A. B. Lidiard, *J. Nucl. Mater.* **19**, 106 (1966).
- ¹⁶H. Kleykamp, *J. Nucl. Mater.* **131**, 221 (1985).
- ¹⁷H. Y. Geng, Y. Chen, Y. Kaneta, and M. Kinoshita, *J. Alloys Compd.* **457**, 465 (2008).
- ¹⁸E. Moore, L. R. Corrales, T. Desai, and R. Devanathan, *J. Nucl. Mater.* **419**, 140 (2011).
- ¹⁹K. Govers, S. E. Lemehov, and M. Verweft, *J. Nucl. Mater.* **374**, 461 (2008).
- ²⁰R. M. Cornell, *Philos. Mag.* **19**, 539 (1969).
- ²¹H. Matzke, *Fission Product Behavior in Ceramic Oxide Fuel* (The American Ceramic Society, Westerville, OH, 1986).
- ²²K. Govers, S. E. Lemehov, and M. Verweft, *J. Nucl. Mater.* **405**, 252 (2010).
- ²³D. A. Andersson, B. P. Uberuaga, P. V. Nerikar, C. Unal, and C. R. Stanek, *Phys. Rev. B* **84**, 054105 (2011).
- ²⁴D. C. Parfitt and R. W. Grimes, *J. Nucl. Mater.* **392**, 28 (2009).
- ²⁵D. Schwen, M. Huang, P. Bellon, and R. S. Averback, *J. Nucl. Mater.* **392**, 35 (2009).
- ²⁶M. Huang, D. Schwen, and R. S. Averback, *J. Nucl. Mater.* **399**, 175 (2010).
- ²⁷K. Govers, C. L. Bishop, D. C. Parfitt, S. E. Lemehov, M. Verweft, and R. W. Grimes, *J. Nucl. Mater.* **420**, 282 (2012).
- ²⁸R. M. Cornell, *J. Nucl. Mater.* **38**, 319 (1971).
- ²⁹C. Baker, *Eur. Appl. Res. Rep., Nucl. Sci. Technol.* **1**, 19 (1979).
- ³⁰A. Michel, C. Sabathier, G. Carlot, O. Kaitasov, Bouffard, and C. Valot, *Nucl. Instrum. Methods Phys. Res. B* **272**, 218 (2012).
- ³¹K. Nogita and K. Une, *Nucl. Instrum. Methods Phys. Res. B* **141**, 481 (1998).
- ³²P. Martin, G. Garcia, P. Carlot, C. Sabathier, C. Valot, V. Nassif, O. Proux, and J.-L. Hazemann, *Nucl. Instrum. Methods Phys. Res. B* **266**, 2887 (2008).
- ³³J.-Y. Oh, Y.-H. Koo, J.-S. Cheon, B.-H. Lee, and D.-S. Sohn, *J. Nucl. Mater.* **372**, 89 (2008).
- ³⁴A. B. Kaplun and A. B. Meshalkin, *Thermophys. Prop. Mater.* **41**, 373 (2003).
- ³⁵C. Ronchi, *J. Nucl. Mater.* **96**, 314 (1981).
- ³⁶T. Xiao-Feng, L. Chong-Sheng, Z. Zheng-He, and G. Tao, *Chin. Phys. B* **19**, 057102 (2010).
- ³⁷C. R. A. Catlow, *Proc. R. Soc. London, Ser. A* **353**, 533 (1977).
- ³⁸M. Abramowski, R. W. Grimes, and S. Owens, *J. Nucl. Mater.* **275**, 12 (1999).
- ³⁹C. B. Basak, A. K. Sengupta, and H. S. Kamath, *J. Alloys Compd.* **360**, 210 (2003).
- ⁴⁰N.-D. Morelon, D. Ghaleb, J.-M. Delaye, and L. V. Brutzel, *Philos. Mag.* **83**, 1533 (2003).
- ⁴¹R. A. Jackson, A. D. Murray, and C. R. A. Catlow, *Philos. Mag. A* **53**, 27 (1986).
- ⁴²G. V. Lewis and C. R. A. Catlow, *J. Phys. C* **18**, 1149 (1985).
- ⁴³C. Meis and J. D. Gale, *Mater. Sci. Eng. A* **57**, 52 (1998).
- ⁴⁴C. Meis and A. Chartier, *J. Nucl. Mater.* **341**, 25 (2005).
- ⁴⁵K. Yamada, K. Kurosaki, M. Uno, and S. Yamanaka, *J. Alloys Compd.* **307**, 10 (2000).
- ⁴⁶T. Arima, S. Yamasaki, Y. Inagaki, and K. Idemitsu, *J. Alloys Compd.* **400**, 43 (2005).
- ⁴⁷K. Govers, S. Lemehov, M. Hou, and M. Verweft, *J. Nucl. Mater.* **366**, 161 (2007).
- ⁴⁸R. Devanathan, J. Yu, and W. J. Weber, *J. Chem. Phys.* **130**, 174502 (2009).
- ⁴⁹L. V. Brutzel, J.-M. Delaye, D. Ghaleb, and M. Rarivomanantsoa, *Philos. Mag.* **83**, 4083 (2003).
- ⁵⁰G. Martin, S. Maillard, L. V. Brutzel, P. Garcia, B. Dorado, and C. Valot, *J. Nucl. Mater.* **385**, 351 (2009).
- ⁵¹C. L. Bishop, R. W. Grimes, and D. C. Parfitt, *Nucl. Instrum. Methods Phys. Res. B* **268**, 2915 (2010).
- ⁵²L. V. Brutzel and M. Rarivomanantsoa, *J. Nucl. Mater.* **358**, 209 (2006).
- ⁵³L. V. Brutzel, E. Vincent-Aublant, and J.-M. Delaye, *Nucl. Instrum. Methods Phys. Res. B* **267**, 3013 (2009).

- ⁵⁴L. Van Brutzel and E. Vincent-Aublant, *J. Nucl. Mater.* **377**, 522 (2008).
- ⁵⁵K. T. Tang and J. P. Toennies, *J. Chem. Phys.* **118**, 4976 (2003).
- ⁵⁶A. Chartier, L. Van Brutzel, and M. Freyss, *Phys. Rev. B* **81**, 174111 (2010).
- ⁵⁷D. Frenkel and B. Smit, *Understanding Molecular Simulation: From Algorithms to Applications* (Academic Press, San Diego, 2001).
- ⁵⁸A. Couet, J.-P. Crocombette, and A. Chartier, *J. Nucl. Mater.* **404**, 50 (2010).
- ⁵⁹B. Widom, *J. Chem. Phys.* **39**, 2808 (1963).
- ⁶⁰M. Freyss (private communication).
- ⁶¹X.-Y. Liu, B. P. Uberuaga, D. A. Andersson, C. R. Stanek, and K. E. Sickafus, *Appl. Phys. Lett.* **98**, 151902 (2011).
- ⁶²K. Govers, S. Lemehov, M. Hou, and M. Verweft, *J. Nucl. Mater.* **366**, 161 (2007).
- ⁶³L. Van Brutzel, A. Chartier, and J. P. Crocombette, *Phys. Rev. B* **78**, 024111 (2008).
- ⁶⁴P. Garcia, P. Martin, G. Carlot, E. Castelier, M. Ripert, C. Sabathier, C. Valot, F. D'Acapito, J. L. Hazemann, O. Proux, and V. Nassif, *J. Nucl. Mater.* **352**, 136 (2006).
- ⁶⁵J. A. Beattie, R. J. Barriault, and J. S. Brierley, *J. Chem. Phys.* **19**, 1219 (1951).
- ⁶⁶A. N. Zisman, I. V. Aleksandrov, and S. M. Stishov, *Phys. Rev. B* **32**, 484 (1985).